ARL-TR-9564 • Sep 2022

DEVCOM ARMY RESEARCH LABORATORY

Automated Gain-Scheduling Approach for Three-Loop Autopilot

by Joshua T Bryson and Benjamin C Gruenwald

NOTICES

Disclaimers

The findings in this report are not to be construed as an official Department of the Army position unless so designated by other authorized documents.

Citation of manufacturer's or trade names does not constitute an official endorsement or approval of the use thereof.

Destroy this report when it is no longer needed. Do not return it to the originator.

ARL-TR-9564 ● SEP 2022

Automated Gain-Scheduling Approach for Three-Loop Autopilot

by Joshua T Bryson and Benjamin C Gruenwald
DEVCOM Army Research Laboratory

REPORT DOCUMENTATION PAGE

Form Approved
OMB No. 0704-0188

PLEASE DO NOT RETURN YOUR FORM TO THE ABOVE ADDRESS.

1. REPORT DATE *(DD-MM-YYYY)*	2. REPORT TYPE	3. DATES COVERED (From - To)
September 2022	Technical Report	3 January–27 May 2022

4. TITLE AND SUBTITLE
Automated Gain-Scheduling Approach for Three-Loop Autopilot

5a. CONTRACT NUMBER

5b. GRANT NUMBER

5c. PROGRAM ELEMENT NUMBER

6. AUTHOR(S)
Joshua T Bryson and Benjamin C Gruenwald

5d. PROJECT NUMBER

5e. TASK NUMBER

5f. WORK UNIT NUMBER

7. PERFORMING ORGANIZATION NAME(S) AND ADDRESS(ES)
DEVCOM Army Research Laboratory
ATTN: FCDD-RLW-WD
Aberdeen Proving Ground, MD 21005

8. PERFORMING ORGANIZATION REPORT NUMBER
ARL-TR-9564

9. SPONSORING/MONITORING AGENCY NAME(S) AND ADDRESS(ES)

10. SPONSOR/MONITOR'S ACRONYM(S)

11. SPONSOR/MONITOR'S REPORT NUMBER(S)

12. DISTRIBUTION/AVAILABILITY STATEMENT
Approved for public release; distribution is unlimited.

13. SUPPLEMENTARY NOTES
primary author's email: <joshua.t.bryson.civ@army.mil>.
ORCID: Joshua Bryson, 0000-0002-0753-6823; Benjamin Gruenwald, 0000-0003-3968-5070

14. ABSTRACT
This report documents an approach to flight control design for guided projectile applications with expanded flight envelopes. This method helps shorten the design-cycle iteration time by streamlining the tuning of gain-schedule surfaces across the flight envelope while simultaneously ensuring desired performance and robustness criteria are satisfied. This methodology is demonstrated on an example high-speed guided projectile to construct an effective gain-schedule across a supersonic flight envelope.

15. SUBJECT TERMS flight control, gain-scheduling, guided projectile, high-speed projectile, nonlinear aerodynamics, robustness, tail-control, Weapons Sciences

16. SECURITY CLASSIFICATION OF:			17. LIMITATION OF ABSTRACT	18. NUMBER OF PAGES	19a. NAME OF RESPONSIBLE PERSON
a. REPORT	b. ABSTRACT	c. THIS PAGE			19b. TELEPHONE NUMBER (Include area code)
Unclassified	Unclassified	Unclassified	UU	48	Joshua T Bryson 410-306-1939

Contents

List of Figures

List of Tables

1. Introduction

The US Army's modernization strategy to enable Multi-Domain Operations (MDO) includes foundational research investments to improve the warfighting capabilities, including a priority research focus into advancements in Long-Range Precision Fires (LRPF), which includes research enabling high-speed/hypersonic Army munitions.[1] The realization of the Army MDO LRPF future concept requires precision guided munitions with improved maneuverability that can operate over an expanded flight envelope to enable range extension and trajectory shaping maneuvers, and engagement of imperfectly located targets.[2–6]

Another emphasis for Army research is developing the ability to more rapidly evolve Army capabilities and accelerate new start programs, enabling a more agile response to changing threat environments. Working toward this desired capability goal, this research develops a methodology to rapidly design effective flight control for high-speed, highly maneuverable guided munitions to enable desired operation across an expanded flight envelope covering a wide range of Mach and dynamic pressure values. Furthermore, Army-relevant LRPF munition concepts often have severe space restrictions for packaging onboard computation, actuation systems, and sensors, and also require overcoming significant challenges such as extreme operating environments (e.g., high thermal loading from low-altitude, hypersonic flight, and/or high mechanical shock from gun launch). These challenges influence sensor and actuator design, and can impose stringent robustness requirements and inhibit the achievable performance of the flight control architectures.

Particularly in the early stages of a new munition design process, it is desirable to quickly update the tuned control gains as the aerodynamics and mass properties evolve. This allows for timely evaluation of closed-loop maneuverability and system performance metrics to provide input for the overall munition development, including the lifting and stabilizing surface sizing, control surface properties, actuation system requirements, and sensor specifications.

This methodology develops a flight control approach that provides effective disturbance rejection and command tracking for a high-speed guided munition across an expanded flight envelope, while prioritizing robustness to modeling uncertainties and maintaining a focus on rapid tuning capability by leveraging available tools for automation. An efficient, systematic approach is used to gain-schedule a three-loop

autopilot, using a set of desired design constraints to enforce performance, stability, and robustness properties. A similar approach for tuning a three-loop autopilot for a missile system is described in Theodoulis and Proff.[7]

2. Projectile Flight Dynamics

In this section, we present the nonlinear flight dynamics for a generic tail-controlled projectile. It should be noted that these dynamic equations follow the formulation of any standard aerial vehicle, which is well known in the literature.[8–11] For this report to be self contained, we include an overview of these nonlinear dynamic equations and how to simplify them into a controllable dynamic model.

2.1 Reference Frames and Kinematic Equations

We begin by introducing the relevant reference frames and coordinate systems needed to describe the position and orientation of the projectile. To start, the following standard assumptions are made: *1) the projectile is rigid, 2) the rotation of the Earth is neglected, 3) the effect of the wind is neglected, and 4) the projectile center-of-mass is located at the center-of-gravity*. Now, we set the Earth reference frame, $\mathcal{R}_{\mathrm{E}} = \{\mathcal{O}_{\mathrm{E}}, x_{\mathrm{E}}, y_{\mathrm{E}}, z_{\mathrm{E}}\}$, as the inertial frame. The coordinate system follows the right-hand rule with the origin ($\mathcal{O}_{\mathrm{E}}$) at the launch location, the x-axis (x_{E}) pointing toward the target centroid, the y-axis (y_{E}) pointing 90° to the east of the x-axis, and the z-axis (z_{E}) pointing down and perpendicular to the xy-plane. The body-fixed reference frame, $\mathcal{R}_{\mathrm{b}} = \{\mathcal{O}_{\mathrm{b}}, x_{\mathrm{b}}, y_{\mathrm{b}}, z_{\mathrm{b}}\}$, is a noninertial frame with a coordinate system fixed at the center-of-gravity location on the body of the projectile. In addition to the origin ($\mathcal{O}_{\mathrm{b}}$) at the center-of-gravity, the coordinate system is designated by the x-axis (x_{b}) pointing through the nose of the projectile, the y-axis (y_{b}) pointing 90° right of the x-axis, and the z-axis (z_{b}) pointing down and perpendicular to the xy-plane. The relation between the Earth frame and body-fixed frame can be visualized in Fig. 1, where the three Euler angles for roll, pitch, and yaw, given by ϕ, θ, and ψ, respectively, describe the angular orientation (or attitude) of the body-fixed frame relative to the Earth frame.

Through a series of angular rotations, the orientation of the body-fixed frame can be given with respect to the fixed Earth reference frame. A "$Z \rightarrow Y \rightarrow X$" Euler

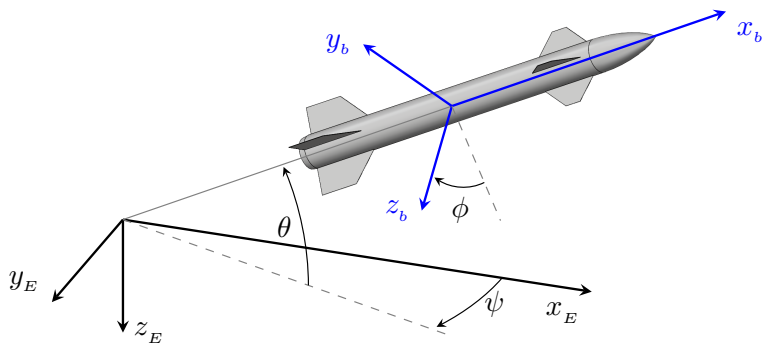

Fig. 1 Illustration of a generic projectile with a body-fixed frame relative to an Earth reference frame (inertial frame)

sequence of rotations is represented by the transformation matrix

$$[\mathbf{T}]^{\mathrm{bE}} = \begin{bmatrix} \mathrm{c}_\theta \mathrm{c}_\psi & \mathrm{s}_\phi \mathrm{s}_\theta \mathrm{c}_\psi - \mathrm{c}_\phi \mathrm{s}_\psi & \mathrm{c}_\phi \mathrm{s}_\theta \mathrm{c}_\psi + \mathrm{s}_\phi \mathrm{s}_\psi \\ \mathrm{c}_\theta \mathrm{s}_\psi & \mathrm{s}_\phi \mathrm{s}_\theta \mathrm{s}_\psi + \mathrm{c}_\phi \mathrm{c}_\psi & \mathrm{c}_\phi \mathrm{s}_\theta \mathrm{s}_\psi - \mathrm{s}_\phi \mathrm{c}_\psi \\ -\mathrm{s}_\theta & \mathrm{s}_\phi \mathrm{c}_\theta & \mathrm{c}_\phi \mathrm{c}_\theta \end{bmatrix}, \tag{1}$$

where $\mathrm{s}_\phi = \sin(\phi)$, $\mathrm{c}_\phi = \cos(\phi)$, and so forth. Using this transformation, the kinematic equations that relate the linear (or translational) body-fixed velocities to the inertial rate of change of translational position can be given by

$$\begin{bmatrix} \dot{x} \\ \dot{y} \\ \dot{z} \end{bmatrix} = [\mathbf{T}]^{\mathrm{bE}} \begin{bmatrix} u \\ v \\ w \end{bmatrix}. \tag{2}$$

Note the states $[x, y, z]^{\mathrm{T}}$ are the center-of-gravity positions relative to the Earth inertial frame along the x_E, y_E, and z_E axes, respectively, implying the time derivatives are the velocities. In addition, $[u, v, w]^{\mathrm{T}}$ are the body-fixed linear velocities along the x_b, y_b, and z_b axes, respectively. Integration of Eq. 2 gives the position of the body-fixed frame relative to the Earth reference frame.

The relationship between the body-fixed angular velocities and the rate of change of the Euler angles is determined by resolving the Euler rates into the body-fixed

reference frame. This follows as

$$\begin{bmatrix} p \\ q \\ r \end{bmatrix} = \underbrace{\begin{bmatrix} 1 & 0 & -\mathrm{s}_\theta \\ 0 & \mathrm{c}_\phi & \mathrm{s}_\phi \mathrm{c}_\theta \\ 0 & -\mathrm{s}_\phi & \mathrm{c}_\phi \mathrm{c}_\theta \end{bmatrix}}_{\equiv J} \begin{bmatrix} \dot{\phi} \\ \dot{\theta} \\ \dot{\psi} \end{bmatrix}, \tag{3}$$

where $[p, q, r]^{\mathrm{T}}$ are the body-fixed angular (or rotational) velocities acting in the roll, pitch, and yaw planes, respectively. Using the inverse of the matrix J in Eq. 3, the relationship can be reversed to determine the Euler rates from the body-fixed angular velocities as

$$\begin{bmatrix} \dot{\phi} \\ \dot{\theta} \\ \dot{\psi} \end{bmatrix} = \begin{bmatrix} 1 & \mathrm{s}_\phi \mathrm{t}_\theta & \mathrm{c}_\phi \mathrm{t}_\theta \\ 0 & \mathrm{c}_\phi & -\mathrm{s}_\phi \\ 0 & \mathrm{s}_\phi / \mathrm{c}_\theta & \mathrm{c}_\phi / \mathrm{c}_\theta \end{bmatrix} \begin{bmatrix} p \\ q \\ r \end{bmatrix}, \tag{4}$$

where $\mathrm{t}_\theta = \tan(\theta)$. Again, it is noted that integration of Eq. 4 provides the attitude (or orientation) of the body-fixed frame relative to the Earth reference frame.

The kinematic equations given by Eqs. 2 and 4 are critical for describing the motion of the projectile (body-fixed frame) in reference to the Earth inertial frame. This includes the position, linear velocities, attitude, and angular velocities. From these equations, one can use guidance and navigation to ensure the projectile is on course for a given target. The main contributor to the flight control development are the equations of motion consisting of the forces and moments acting on the projectile. These dictate the body-fixed flight dynamics and are discussed in the next subsection.

First, we introduce one more reference frame, the wind frame, which is commonly used for aerodynamic modeling and flight control development. The wind frame is defined by the instantaneous orientation of the relative wind velocity vector with respect to the body-fixed frame. This can also be thought of as the projectile's center-of-gravity velocity vector being defined with respect to the Earth reference frame with no wind, denoted as $\vec{V} \equiv \vec{V}_{CG/E}$. One can then think of the relative wind vector as $-\vec{V}$ and the airspeed as $V = |\vec{V}|$. Based on this, the wind reference frame, $\mathcal{R}_{\mathrm{w}} = \{\mathcal{O}_{\mathrm{w}}, x_{\mathrm{w}}, y_{\mathrm{w}}, z_{\mathrm{w}}\}$, has the coordinate system with the origin $\mathcal{O}_{\mathrm{w}}$ at the center-of-gravity of the projectile body, the x-axis (x_{w}) is superimposed on the projectile's

center-of-gravity velocity vector V, the z-axis (z_{w}) points 90° down from the x-axis, and the y-axis (y_{w}) completes the right-hand rule. Figure 2 depicts the relationship between the wind frame and the body-fixed frame through the aerodynamic angles (or incidence angles): angle of attack, α, and angle of sideslip, β.

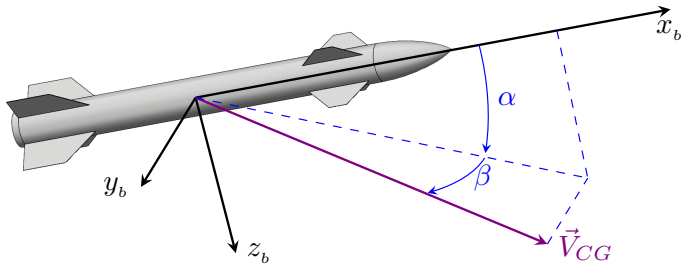

Fig. 2 Wind reference frame relative to the body-fixed reference frame. Angle of attack and angle of sideslip relate to the projectile's center-of-gravity velocity vector.

Rotating along the aerodynamic angles, the body-fixed reference frame is related to the wind reference frame with the transformation matrix give by

$$[\mathbf{T}]^{\mathrm{wb}} = \begin{bmatrix} \mathrm{c}_\alpha \mathrm{c}_\beta & -\mathrm{c}_\alpha \mathrm{s}_\beta & -\mathrm{s}_\alpha \\ \mathrm{s}_\beta & \mathrm{c}_\beta & 0 \\ \mathrm{s}_\alpha \mathrm{c}_\beta & -\mathrm{s}_\alpha \mathrm{s}_\beta & \mathrm{c}_\alpha \end{bmatrix}, \tag{5}$$

where $\mathrm{s}_\alpha = \sin(\alpha)$, $\mathrm{c}_\alpha = \cos(\alpha)$, and so forth. Using this transformation, the body-fixed component velocities can be obtained from the center-of-gravity velocity vector as

$$\begin{bmatrix} u \\ v \\ w \end{bmatrix} = [\mathbf{T}]^{\mathrm{wb}} \begin{bmatrix} V \\ 0 \\ 0 \end{bmatrix} = \begin{bmatrix} V\mathrm{c}_\alpha \mathrm{c}_\beta \\ V\mathrm{s}_\beta \\ V\mathrm{s}_\alpha \mathrm{c}_\beta \end{bmatrix}. \tag{6}$$

As noted previously, V is the airspeed of the projectile and as the magnitude of the velocity vector $\vec{V}$, it can be written as

$$V = \sqrt{u^2 + v^2 + w^2}. \tag{7}$$

Using Eq. 6, the aerodynamic angles can be written in terms of the body-fixed component velocities as

$$\alpha = \arctan\left(\frac{w}{u}\right), \tag{8}$$

$$\beta = \arcsin\left(\frac{v}{V}\right), \tag{9}$$

It is important to note the wind frame as it provides a relationship from the body-fixed frame to the center-of-gravity velocity vector of the projectile (relative to the Earth reference frame). Aerodynamic modeling determines the aerodynamic coefficients related to the forces and moment acting on the body. This is done with respect to the relative wind velocity vector. These coefficients are then related back to the body-fixed frame using the aerodynamic (or incidence) angles. This is used in the next subsection when discussing the aerodynamic coefficients and obtaining them.

2.2 Body-Fixed Flight Dynamics

The projectile flight dynamics are based on the standard rigid body 6-degree-of-freedom equations of motion. To begin, the three linear (or translational) degrees of freedom are governed by Newton's second law with a flat Earth assumption. In vector notation, this is expressed in a general form as

$$\vec{F} = m\frac{\mathrm{d_E}\vec{V}}{\mathrm{d}t} = m\Big[\frac{\mathrm{d_b}\vec{V}}{\mathrm{d}t} + \vec{\omega}_{\mathrm{bE}} \times \vec{V}\Big], \tag{10}$$

where $\vec{F}$ is the vector sum of external forces acting on the projectile, m is the mass of the projectile, $\vec{V}$ is the linear velocity vector of the projectile center-of-gravity with respect to the Earth, $\mathrm{d_E}\vec{V}/\mathrm{d}t$ and $\mathrm{d_b}\vec{V}/\mathrm{d}t$ are the Earth reference frame and body-fixed frame time derivatives, respectively, and $\vec{\omega}_{\mathrm{bE}}$ is the angular velocity of the body-fixed frame with respect to the Earth reference frame.

The external forces acting on the projectile consist of aerodynamic forces and a gravitational force* resolved into the body coordinates. Since the gravitational acceleration is in the Earth frame and points down along the z_E axis, it follows that $g_{\mathrm{E}} = [0, 0, g]^{\mathrm{T}}$. To express the gravitational acceleration in the body-fixed frame, the transformation matrix given by Eq. 1 is used to project from the Earth reference frame to the body-fixed frame as $g_{\mathrm{b}} = [\mathbf{T}]^{\mathrm{bE}} g_{\mathrm{E}} = [-g\mathrm{s}_\theta, g\mathrm{s}_\phi\mathrm{c}_\theta, g\mathrm{c}_\phi\mathrm{c}_\theta]^{\mathrm{T}}$. Now, resolving Eq. 12 in the body-fixed frame with the vector components defined as $\vec{V} = [u, v, w]^{\mathrm{T}}$, $\vec{\omega}_{\mathrm{bE}} = [p, q, r]^{\mathrm{T}}$, and $\vec{F} = [F_X, F_Y, F_Z]^{\mathrm{T}} + mg_{\mathrm{b}}$, the expression for linear velocity dynamics in the body-fixed frame can be written as

*When considering a more general aerial vehicle, one would also include a thrust force acting on the flight body from propulsive components. Projectiles, in general, do not have propulsive components so the thrust force can be neglected. However, it should be noted that the proposed flight control framework can be implemented regardless of the inclusion or exclusion of a thrust force component.

$$\begin{bmatrix} \dot{u} \\ \dot{v} \\ \dot{w} \end{bmatrix} = \frac{1}{m} \begin{bmatrix} F_X - mg\mathrm{s}_\theta \\ F_Y + mg\mathrm{s}_\phi \mathrm{c}_\theta \\ F_Z + mg\mathrm{c}_\phi \mathrm{c}_\theta \end{bmatrix} - \begin{bmatrix} 0 & -r & q \\ r & 0 & -p \\ -q & p & 0 \end{bmatrix} \begin{bmatrix} u \\ v \\ w \end{bmatrix}. \tag{11}$$

The three angular (or rotational) degrees of freedom are governed by Euler's law with a flat Earth assumption. In vector notation, this is expressed in a general form as

$$\dot{\vec{\omega}}_{\mathrm{bE}} = \vec{I}^{-1}\Big[\vec{M} - \vec{\omega}_{\mathrm{bE}} \times \vec{I}\vec{\omega}_{\mathrm{bE}}\Big], \tag{12}$$

where $\vec{I}$ is the inertia matrix of the projectile, $\vec{I}\vec{\omega}_{\mathrm{bE}}$ is the angular momentum of the body-fixed frame with respect to the Earth reference frame, and $\vec{M}$ is the vector sum of external moments acting on the projectile.

Since most projectile bodies are symmetric, the inertia matrix can be simplified to contain only diagonal elements $\vec{I} = \mathrm{diag}([I_x, I_y, I_z])$ and with the body components of angular rates $\vec{\omega}_{\mathrm{bE}} = [p, q, r]^{\mathrm{T}}$ and external moments* $\vec{M} = [M_l, M_m, M_n]^{\mathrm{T}}$, the expression for angular velocity dynamics in the body-fixed frame can be written as

$$\begin{bmatrix} \dot{p} \\ \dot{q} \\ \dot{r} \end{bmatrix} = \begin{bmatrix} I_x^{-1} & 0 & 0 \\ 0 & I_y^{-1} & 0 \\ 0 & 0 & I_z^{-1} \end{bmatrix} \begin{bmatrix} M_l \\ M_m \\ M_n \end{bmatrix} + \begin{bmatrix} I_x^{-1}(I_y - I_z)qr \\ I_y^{-1}(I_z - I_x)pr \\ I_z^{-1}(I_x - I_y)pq \end{bmatrix}. \tag{13}$$

2.3 Aerodynamic Modeling from Forces and Moments

The aerodynamic forces and moments acting on the projectile flight body are expressed in the body-fixed frame with the aerodynamic forces consisting of an axial, side, and normal force and the aerodynamic moments consist of a rolling, pitching, and yawing moment. These are written respectively as

*The sole contribution to the external moments are the aerodynamic moments. Owing to the assumption that the center-of-mass is located at the center-of-gravity, there is no moment due to the gravitational force. Furthermore, since there is no propulsive component acting on the projectile, there is no moment contribution from a thrust force. Once again, the proposed flight control framework can be implemented regardless of the inclusion or exclusion of a thrust force component and the resulting moment.

$$\begin{bmatrix} F_X \\ F_Y \\ F_Z \end{bmatrix} = QS \begin{bmatrix} C_X \\ C_Y \\ C_Z \end{bmatrix}, \quad \begin{bmatrix} M_l \\ M_m \\ M_n \end{bmatrix} = QSD \begin{bmatrix} C_l \\ C_m \\ C_n \end{bmatrix}, \tag{14}$$

where $Q = \frac{1}{2}\rho V^2$ is the dynamic pressure (V being the airspeed and ρ being the air density), $S = \frac{\pi}{4}D^2$ is the aerodynamic reference area, D is the projectile diameter, and C_X, C_Y, C_Z, C_l, C_m, and C_n are nondimensional force and moment coefficients.

An aerodynamic model can be used to provide the aerodynamic forces and moments resulting in the aerodynamic coefficient data.[11,12] The aerodynamic coefficients are dependent on the flight conditions of the projectile and can be given as functions of Mach number, aerodynamic angles, body-fixed angular rates, and the aerodynamic virtual control surface deflections. This can be expressed as

$$C_X = C_X\big(\mathrm{M}, \alpha, \beta, \delta_p\big), \tag{15}$$
$$C_Y = C_Y\big(\mathrm{M}, \beta, \frac{D}{2V}r, \delta_r\big), \tag{16}$$
$$C_Z = C_Z\big(\mathrm{M}, \alpha, \frac{D}{2V}q, \delta_q\big), \tag{17}$$
$$C_l = C_l\big(\mathrm{M}, \alpha, \beta, \frac{D}{2V}p, \delta_p\big), \tag{18}$$
$$C_m = C_m\big(\mathrm{M}, \alpha, \frac{D}{2V}q, \delta_q\big), \tag{19}$$
$$C_n = C_n\big(\mathrm{M}, \beta, \frac{D}{2V}r, \delta_r\big). \tag{20}$$

Each of the aerodynamic coefficients can be extended; however, for the purposes of this report, we expand only the coefficients for the normal force and pitching moment. Specifically, Eqs. 17 and 19 can be written as

$$\begin{aligned} C_Z = {} & C_{Z_0}(\mathrm{M}) + C_{Z_\alpha}(\mathrm{M})\sin\alpha + C_{Z_{\alpha^2}}(\mathrm{M})\sin^2\alpha + C_{Z_{\alpha^3}}(\mathrm{M})\sin^3\alpha \\ & + C_{Z_{\alpha^4}}(\mathrm{M})\sin^4\alpha + C_{Z_{\alpha^5}}(\mathrm{M})\sin^5\alpha + \frac{D}{2V}C_{Z_q}(\mathrm{M})q \\ & + C_{Z_{\delta_q}}(\mathrm{M},\alpha)\delta_q, \end{aligned} \tag{21}$$

$$\begin{aligned} C_m = {} & C_{m_0}(\mathrm{M}) + C_{m_\alpha}(\mathrm{M})\sin\alpha + C_{m_\alpha^2}(\mathrm{M})\sin^2\alpha + C_{m_\alpha^3}(\mathrm{M})\sin^3\alpha \\ & + C_{m_\alpha^4}(\mathrm{M})\sin^4\alpha + C_{m_{\alpha^5}}(\mathrm{M})\sin^5\alpha + \frac{D}{2V}C_{m_q}(\mathrm{M})q \\ & + C_{m_{\delta_q}}(\mathrm{M},\alpha)\delta_q. \end{aligned} \tag{22}$$

The dynamic component on the normal force coefficient given by $C_{Z_q}(\mathrm{M})qD/2V$ is negligible and the static components given by the $\sin(\cdot)$ functions and nominal terms C_{Z_0} and C_{m_0} can be represented instead as a function of α. We then write Eqs. 21 and 22 as

$$C_Z = C_{Z_\alpha}(\mathrm{M},\alpha)\alpha + C_{Z_{\delta_q}}(\mathrm{M},\alpha)\delta_q, \tag{23}$$

$$C_m = C_{m_\alpha}(\mathrm{M},\alpha)\alpha + \frac{D}{2V}C_{m_q}(\mathrm{M})q + C_{m_{\delta_q}}(\mathrm{M},\alpha)\delta_q. \tag{24}$$

Here we note that the coefficients C_{Z_α}, C_{m_α}, and C_{m_q} are referred to as stability or aerodynamic derivatives as they notate derivatives taken with respect to α and q (i.e., $C_{Z_\alpha} = \mathrm{d}C_Z/\mathrm{d}\alpha$, $C_{m_\alpha} = \mathrm{d}C_m/\mathrm{d}\alpha$, $C_{m_q} = \mathrm{d}C_m/\mathrm{d}q$). Similarly, the coefficients $C_{Z_{\delta_q}} = \mathrm{d}C_Z/\mathrm{d}\delta_q$ and $C_{m_{\delta_q}} = \mathrm{d}C_m/\mathrm{d}\delta_q$ are referred to as control derivatives.

As mentioned previously, all the force and moment coefficients can be further expanded into separate static and dynamic components with stability and control derivatives specific to the given axes of motion. These aerodynamic terms are obtained using a combination of semi-empirical aero prediction tools, as well as inviscid and Navier–Stokes computational fluid dynamics (CFD) and wind tunnel measurements and are then organized in look-up tables across a flight envelope of operation.[13] For example, Fig. 3, provided later in Section 3, depicts the variation of the stability and control derivatives from Eqs. 23 and 24. We specifically use the coefficients for the normal force and pitching moment as they are used in the next section to produce a linear system for the proposed flight control framework.

3. Flight Control Methodology

The previous section provided details on the full 6-degree-of-freedom equations of motion for a projectile. These equations are nonlinear by nature and capture the cross-coupling between the different planes of motion. In addition, the process of obtaining aerodynamic information to model the forces and moments acting on the projectile was briefly highlighted. Understanding the motion of the projectile in flight from the dynamics and using the aerodynamic coefficients specific to a given flight body, one can design an appropriate flight control.

It is common practice to make assumptions and simplify the flight dynamics and then design a flight control that is robust enough to account for the simplifications. This can be done by assuming small angles and neglecting cross-coupling terms

such that a linearized model of the flight dynamics can be achieved. The control gains are tuned around many operating conditions with this linear model to cover an entire flight envelope. A gain-schedule is constructed from these tuned control gains such that the projectile is properly controlled within the entire flight envelope. This process can be very time intensive if the control gains are manually tuned for hundreds of operating conditions.

Thus, the objective in this work is to propose a flight control design methodology that prioritizes robustness to model inaccuracies and simplifying assumptions while leveraging available tools for automation to reduce the design cycle iteration time. This approach is applicable to a wide variety of applications and controller architectures. For this report, we consider a generic tail-controlled projectile[2–6,14–18] and use this methodology to design a longitudinal flight control.

3.1 Flight Control Model Linearization

It is common practice to decouple the flight control for the different planes of motion (i.e., longitudinal in the pitch plane and lateral-directional in the roll and yaw planes). The longitudinal dynamics can be described by the time evolution of the states $[u, w, q, \theta]$. These dynamics can be categorized into the short-period motion and the long-period (or phugoid) motion. In this work, the short-period approximation of the projectile is considered for the flight control development. The short-period dynamics are described by the aerodynamic angle and the body angular rate in the pitch-plane of motion (i.e., the angle of attack α and the pitch rate q).

Noting from Eq. 8, the angle of attack is dependent on u and w, we start by differentiating both sides of the equation to obtain the time rate of change for angle of attack as

$$\dot{\alpha} \;=\; \frac{u\dot{w} - w\dot{u}}{u^2 + w^2} \tag{25}$$

Now, using the body-fixed velocity components, u, v, and w, given by Eq. 6 and $\dot{u}$ and $\dot{w}$ given in Eq. 11, one can use several algebraic steps to write Eq. 25 as

$$\begin{aligned}\dot{\alpha} \;=\;& q - (p\mathrm{c}_\alpha + r\mathrm{s}_\alpha)\mathrm{t}_\beta + \frac{1}{mV\mathrm{c}_\beta}\big[(F_Z + mg\mathrm{c}_\phi\mathrm{c}_\theta)\mathrm{c}_\alpha \\ & -(F_X - mg\mathrm{s}_\theta)\mathrm{s}_\alpha\big]\end{aligned} \tag{26}$$

By assuming the aerodynamic angles and the roll and yaw rates remain small*, neglecting gravity, and using the appropriate relation from Eq. 14, this can be written as

$$\dot{\alpha} \;=\; q + \frac{QS}{mV} C_Z. \tag{27}$$

Pulling $\dot{q}$ from Eq. 13, neglecting the cross-coupling of the body-fixed angular rates, and using the appropriate relation from Eq. 14, we obtain

$$\dot{q} \;=\; \frac{QSD}{I_y} C_m. \tag{28}$$

In addition, since the control objective will be to follow a desired acceleration command, we note here that the projectile's specific vertical acceleration $A_Z = -F_Z/m$ can be written as

$$A_Z \;=\; -\frac{QS}{m} C_Z, \tag{29}$$

where the negative sign is used by convention so a positive angle of attack supplies a positive vertical acceleration.

Using the expressions for the force and moment coefficients given by Eqs. 23 and 24, we can write Eqs. 27 and 28 in terms of the Mach and angle-of-attack dependent stability and control derivatives as

$$\dot{\alpha} \;=\; \frac{QS}{mV} C_{Z_\alpha}(\mathrm{M}, \alpha)\alpha + q + \frac{QS}{mV} C_{Z_{\delta_q}}(\mathrm{M}, \alpha)\delta_q, \tag{30}$$

$$\begin{aligned} \dot{q} \;=\; & \frac{QSD}{I_y} C_{m_\alpha}(\mathrm{M}, \alpha)\alpha + \frac{QSD}{I_y}\frac{D}{2V} C_{m_q}(\mathrm{M}) q \\ & + \frac{QSD}{I_y} C_{m_{\delta_q}}(\mathrm{M}, \alpha)\delta_q. \end{aligned} \tag{31}$$

In a similar fashion, the specific vertical acceleration follows as

$$A_Z \;=\; -\frac{QS}{m} C_{Z_\alpha}(\mathrm{M}, \alpha)\alpha - \frac{QS}{m} C_{Z_{\delta_q}}(\mathrm{M}, \alpha)\delta_q. \tag{32}$$

At this point, the short-period dynamics have been simplified into a linear form that is dependent on the stability and control derivatives, which are nonlinear functions

*This can be viewed as fixing the projectile in the pitch plane of motion.

of Mach and angle of attack.

For the considered example tail-controlled projectile, we use the flight envelope, Ξ, defined by

$$\Xi = \begin{cases} 1.2 \leq \mathrm{M} \leq 3.8 \\ |\alpha| \leq 12^{\circ} \\ \text{Sea Level.} \end{cases}$$

Across this flight envelope, the stability and control derivatives for the short-period dynamics for the example projectile can be seen in Fig. 3. It is clear they vary significantly across the flight envelope, and are nonlinear in Mach and angle of attack.

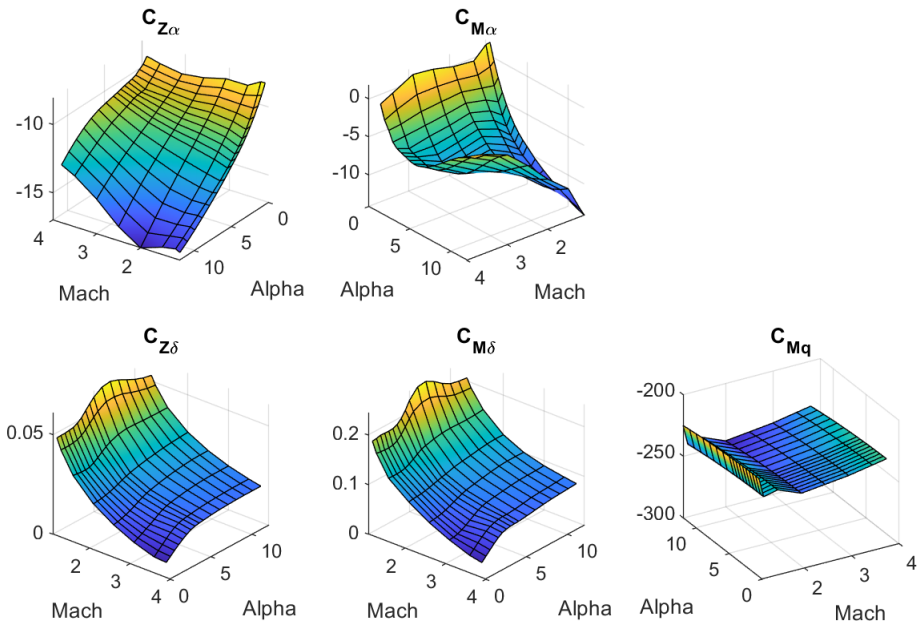

Fig. 3 Stability and control derivatives varying across flight envelope

The nonlinearity of the coefficients motivates a gain-scheduling approach to the flight control design. To implement this approach, the flight envelope, Ξ, is discretized into sample points, $\xi = [\mathrm{M}, \alpha] \in \Xi$. The short-period dynamics for the projectile are then evaluated at each ξ to build a family of linear models scheduled across the flight envelope. To see this, we augment the short-period dynamics given by Eqs. 30 and 31 and compactly write them along with the specific vertical

acceleration in the state-space form

$$\begin{bmatrix} \dot{\alpha} \\ \dot{q} \end{bmatrix} = \underbrace{\begin{bmatrix} \frac{Z_\alpha(\xi)}{V} & 1 \\ M_\alpha(\xi) & M_q(\xi) \end{bmatrix}}_{A(\xi)} \underbrace{\begin{bmatrix} \alpha \\ q \end{bmatrix}}_{x} + \underbrace{\begin{bmatrix} \frac{Z_{\delta_q}(\xi)}{V} \\ M_{\delta_q}(\xi) \end{bmatrix}}_{B(\xi)} \delta_q \tag{33}$$

$$\underbrace{\begin{bmatrix} q \\ A_Z \end{bmatrix}}_{y} = \underbrace{\begin{bmatrix} 0 & 1 \\ -Z_\alpha(\xi) & 0 \end{bmatrix}}_{C(\xi)} \begin{bmatrix} \alpha \\ q \end{bmatrix} + \underbrace{\begin{bmatrix} 0 \\ -Z_{\delta_q}(\xi) \end{bmatrix}}_{D(\xi)} \delta_q \tag{34}$$

The terms within the state-space matrices in Eqs. 33 and 34 are now represented as dimensional derivatives terms for convenience. Table 1 is provided for reference.

Table 1 Dimensional derivative terms

$Z_\alpha = \frac{QS}{m} C_{Z_\alpha}$	$Z_\delta = \frac{QS}{m} C_{Z_{\delta_q}}$
$M_\alpha = \frac{QSD}{I_y} C_{m_\alpha}$	$M_q = \frac{QSD}{I_y} \frac{D}{2V} C_{m_q}$
$M_\delta = \frac{QSD}{I_y} C_{m_{\delta_q}}$	

The dimensional derivative terms within the state-space matrices for this example projectile can be evaluated at each discretized sample point $\xi = [\mathrm{M}, \alpha] \in \Xi$, as shown in Fig. 4, with subscripts corresponding to the matrix row, column indices, as shown:

$$\begin{aligned} \dot{x} &= \begin{bmatrix} A_{11}(\xi) & 1 \\ A_{21}(\xi) & A_{22}(\xi) \end{bmatrix} x + \begin{bmatrix} B_{11}(\xi) \\ B_{21}(\xi) \end{bmatrix} \delta_q \\ y &= \begin{bmatrix} 0 & 1 \\ C_{21}(\xi) & 0 \end{bmatrix} x + \begin{bmatrix} 0 \\ D_{21}(\xi) \end{bmatrix} \delta_q \end{aligned} \tag{35}$$

If a Simulink model of the nonlinear system dynamics is available, an alternative approach to model linearization is available through a MATLAB/Simulink workflow. In this approach, the `operspec` command is used to first define operating point specifications for each ξ, and then the `findop` command is used to trim the Simulink model at each operating point. The trimmed model is then linearized at each operating point using the `linearize` command. The linearized models can then be reformulated as needed to match the form of Eq. 35.

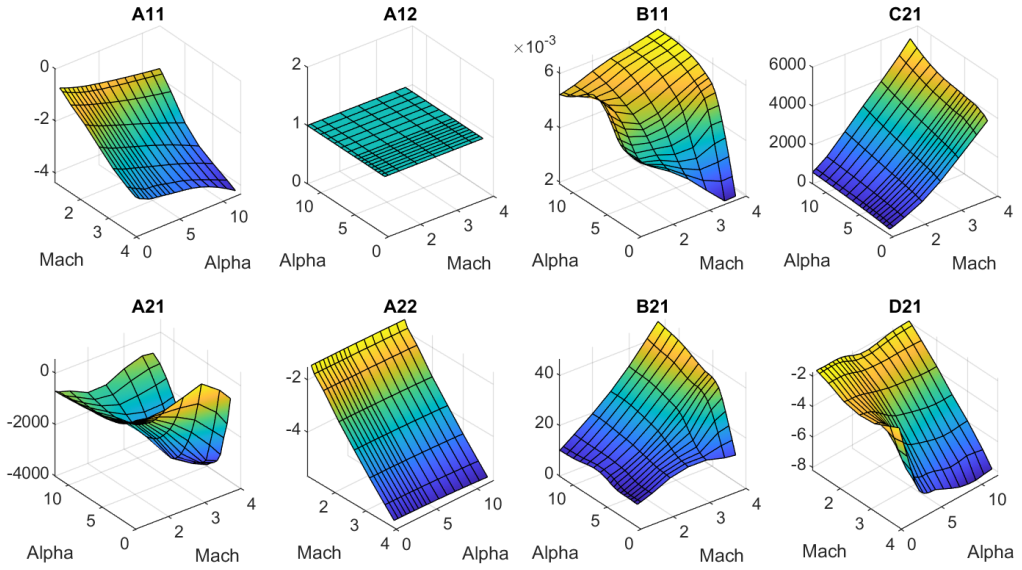

Fig. 4 Short-period approximation linear model terms varying across flight envelope

3.2 Actuator Model

The actuator dynamics are important to consider in the flight control tuning process, as slower actuators interfere with the ability of the flight control to access the projectile dynamics. In this example, the actuators are modeled as a standard second-order system, as shown in Eq. 36:

$$\begin{bmatrix} \dot{\delta}_q \\ \ddot{\delta}_q \end{bmatrix} = \begin{bmatrix} 0 & 1 \\ -\omega_{\mathrm{n}}^2 & -2\zeta\omega_{\mathrm{n}} \end{bmatrix} \begin{bmatrix} \delta_q \\ \dot{\delta}_q \end{bmatrix} + \begin{bmatrix} 0 \\ \omega_{\mathrm{n}}^2 \end{bmatrix} \delta_q^{\mathrm{cmd}}, \tag{36}$$

where the damping ratio, ζ, and the actuator natural frequency, ω_{n}, are chosen as 0.707 and 300 rad/s, respectively, for this example.

3.3 Flight Control Design

The performance objective for the flight controller in this example is to provide tracking of vertical acceleration command and improve disturbance rejection across the expanded flight envelope Ξ. The flight control design is complicated by the aerodynamic nonlinearities of the projectile and unstable dynamics at low α.[16] A three-loop controller design is chosen for this example, as illustrated in Fig. 5. The

controller can be expressed with the following dynamics

$$\begin{bmatrix} \dot{x}_{\mathrm{i}} \\ \dot{\delta}_q^{\mathrm{cmd}} \end{bmatrix} = \begin{bmatrix} 0 & 0 \\ K_u K_q K_i & -K_u \end{bmatrix} \begin{bmatrix} x_{\mathrm{i}} \\ \delta_q^{\mathrm{cmd}} \end{bmatrix} + \begin{bmatrix} K_a & -K_a & -1 \\ K_u K_e & -K_u K_e & -K_u K_q \end{bmatrix} \begin{bmatrix} A_Z^{\mathrm{ref}} \\ A_Z \\ q \end{bmatrix} \tag{37}$$

where the pitch deflection command, δ_q^{cmd}, is used to track the vertical acceleration reference signal, A_Z^{ref}, using feedback of A_Z and q, which are the measured body acceleration and pitch rate, respectively.[7] This controller design provides four tunable gains, K_a, K_i, K_q, and K_e, as well as a low-pass output filter set by K_u. The output filter is chosen based on the actuator dynamics and helps ensure the closed-loop system is protected from actuator modeling uncertainty. In this approach, the four tunable gains are calculated using an optimization process that attempts to ensure a desired set of performance goals are met.

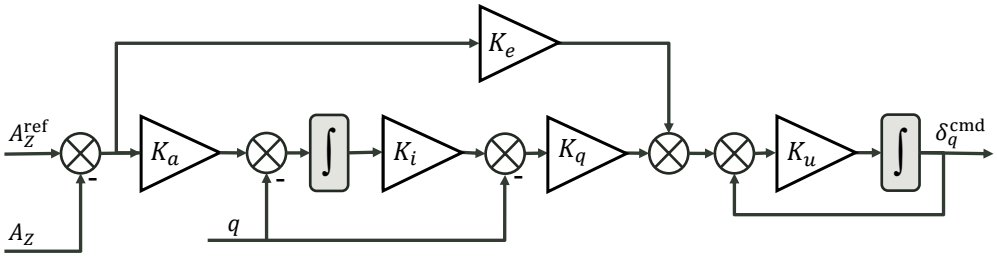

Fig. 5 Diagram of the three-loop controller for the longitudinal projectile dynamics

3.4 Closed-Loop Model

The controller dynamics given by Eq. 37 can be augmented with the actuator dynamics in Eq. 36 and the short-period approximation dynamics given by Eq. 35 to be written in a closed-loop form, letting $x_{\mathrm{cl}} = [\alpha, q, \delta_q, \dot{\delta}_q, x_{\mathrm{i}}, \delta_q^{cmd}]^{\mathrm{T}}$ and $y_{\mathrm{cl}} = [\alpha, q, A_z]^{\mathrm{T}}$,

$$\dot{x}_{\mathrm{cl}} = A_{\mathrm{cl}} x_{\mathrm{cl}} + B_{\mathrm{cl}} A_Z^{\mathrm{ref}} \tag{38}$$

$$y_{\mathrm{cl}} = C_{\mathrm{cl}} x_{\mathrm{cl}}$$

where

$$A_{\text{cl}} = \begin{bmatrix} A_{11}(\xi) & A_{12}(\xi) & B_{11}(\xi) & 0 & 0 & 0 \\ A_{21}(\xi) & A_{22}(\xi) & B_{21}(\xi) & 0 & 0 & 0 \\ 0 & 0 & 0 & 1 & 0 & 0 \\ 0 & 0 & -\omega_{\text{n}}^2 & -2\zeta\omega_{\text{n}} & 0 & \omega_{\text{n}}^2 \\ -K_a C_{21}(\xi) & -1 & -K_a D_{21}(\xi) & 0 & 0 & 0 \\ -K_u K_e C_{21}(\xi) & -K_u K_q & -K_u K_e D_{21}(\xi) & 0 & K_u K_q K_i & -K_u \end{bmatrix},$$

$$B_{\text{cl}} = \begin{bmatrix} 0 \\ 0 \\ 0 \\ 0 \\ K_a \\ K_u K_e \end{bmatrix}, \quad \text{and} \quad C_{\text{cl}} = \begin{bmatrix} 1 & 0 & 0 & 0 & 0 & 0 \\ 0 & 1 & 0 & 0 & 0 & 0 \\ C_{21}(\xi) & 0 & D_{21}(\xi) & 0 & 0 & 0 \end{bmatrix}.$$

This system describes the dynamics of the controlled plant across the flight envelope, as a function of the choice of controller gains, K_a, K_i, K_q, and K_e, K_u, and is used in the optimization process to choose gain values that result in desirable closed-loop system performance.

4. Tuning Approach

For the tuning process of the gain-scheduled three-loop autopilot, this methodology uses defined tuning goals/constraints to achieve desired performance and robustness metrics. Optimization tools within MATLAB are then used to identify the control gains across the entire flight envelope that satisfy the given constraints. This approach prioritizes rapid tuning capability by leveraging available tools for automation while resulting in a controller that has desired performance and robustness properties.

The closed-loop system model from Eq. 38 describes the dynamics of the controlled plant across the flight envelope as a function of the choice of controller gains. For this example, K_u is chosen to be 250 rad/s, based on the actuator bandwidth of 300 rad/s. This choice sets the roll-off filter for the controller slower than the actuator to include margin for actuator uncertainty. The K_a, K_i, K_q, and K_e gains are defined as smoothly varying polynomial surfaces across the flight envelope, according to the form of Eq. 39.

$$K(M,\alpha) = k_0 + k_1 M + k_2 \alpha + k_3 \alpha M + k_4 \alpha^2 + k_5 \alpha^2 M + k_6 \alpha^3 \qquad (39)$$

These tunable gain surfaces are defined in MATLAB using the `tunableSurface` function, enabling the MATLAB to adjust each k_i coefficient within the optimization. Various tuning goals are defined to describe the desired performance and stability characteristics for the controller, and these goals are used to constrain the tuning of the gain surfaces K_a, K_i, K_q, and K_e within the optimization.

4.1 Tuning Goals

The tuning goals in this methodology are governed by the desired crossover frequency for the closed-loop system, ω_c^{FC} to customize speed of desired response. This parameter defines the transition point between low-frequency reference signals the system should track and high-frequency noise the system should suppress. The choice of this single parameter provides a convenient adjustment mechanism to scale the tuning goals to achieve a more conservative (slower) or aggressive (faster) response from the tuned closed-loop system.

An appropriate choice of ω_c^{FC} depends on the dynamics of the combined open-loop plant, which contains all significant dynamics in the system outside the controller itself, including the projectile dynamics, the actuator dynamics, estimator/filter dynamics, and computation delays. Combined plant dynamics with faster frequencies generally allow faster feasible ω_c^{FC} choices.

One major driver of combined plant dynamics is the projectile natural frequency and damping. Driving a plant faster than its natural frequency requires increasingly more control effort, resulting in higher controller gains and increased actuator demands, which can diminish the controller robustness. The actuator response can also severely limit the feasible ω_c^{FC} value. The actuator dynamics break the direct connection between the controller and the system dynamics. Slow actuators interfere more with the ability of the controller to access the system dynamics and apply the proper control signal.

The example projectile used to illustrate this methodology is very lightly damped ($\zeta < 0.1$), with a natural frequency that varies between 20–60 rad/s across the flight envelope, as shown in Fig. 6. From Section 3, recall the actuator frequency for this example is 300 rad/s. With this information, the projectile natural frequency, and

some trial-and-error, the ω_c^{FC} is chosen to vary from 8–20 rad/s for this example, scaling with Mach, as shown in Fig. 7. A single ω_c^{FC} target value may be sufficient for many cases, depending on application specifics and desired performance, but a varying ω_c^{FC} was chosen for this example to illustrate flexibility within the design process.

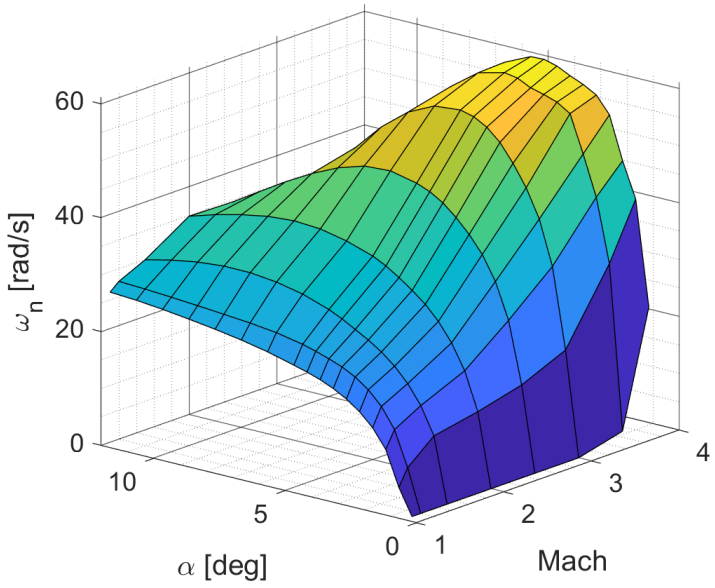

Fig. 6 Natural frequency of the example projectile

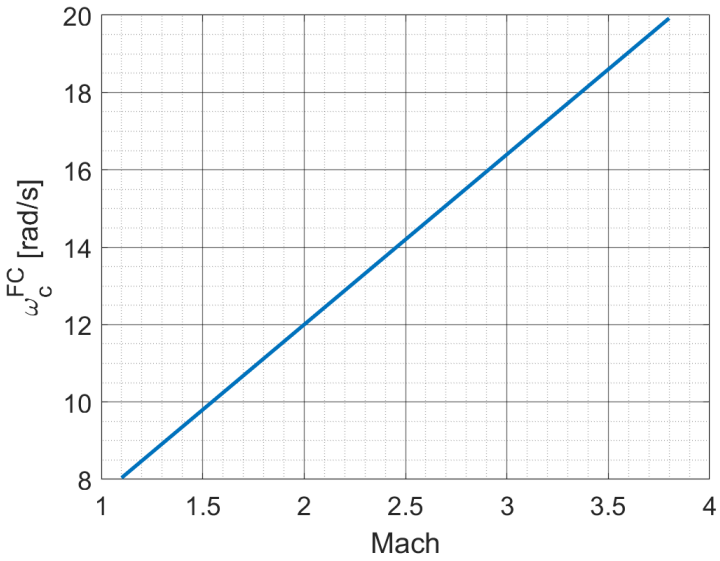

Fig. 7 Desired ω_c^{FC} across the Mach range

This choice of ω_c^{FC} is used to define *hard constraints* and *soft constraints* on the optimization. The methodology uses hard constraints on stability margin and loop shape, which are strictly enforced to ensure desired robustness and performance criteria. Once the hard constraints are satisfied, a soft constraint on reference tracking is used to optimize the tracking response within the hard constraint limits. This process is detailed in the following sections.

4.1.1 Stability Margin

The methodology enforces a *hard constraint* on stability margins within the optimization. Depending on the application, the control system designer can choose from among these stability margin metrics to trade between robustness and performance. In this example, the closed-loop system is subjected to simultaneous gain and phase variations across all plant inputs and outputs to obtain the multiloop input/output disk margin, as illustrated in Fig. 8.

An example stability margin plot is shown in Fig. 9, which plots the loop-at-a-time margins for variation on individual plant outputs, A_Z and q, in blue and red, respectively, along with the margins for variation on the input, δ_q^{cmd}, shown in yellow. The multiloop output margin is shown in purple, obtained by simultaneous variation of gain and phase for both A_Z and q, while the most conservative robustness metric, the multiloop input/output disk margin, is shown in green.

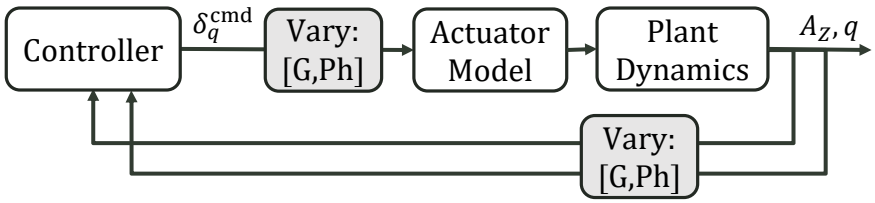

Fig. 8 Stability margin analysis. In this block diagram, "G" denotes gain and "Ph" denotes phase.

For this flight control design example, the design goal for the majority of the flight envelope is defined as 3 dB of gain margin with 30^o phase margin for the multiloop input/output disk margin, as shown in Table 2. The unstable, low-α regions are given a relaxed margin constraint of 2 dB of gain margin with 15^o phase margin to facilitate the tuning process. Enforcement of this tuning goal ensures stability across the flight envelope with significant margin for robustness to plant uncertainty.

This design goal is implemented using the `TuningGoal.Margins` function with-

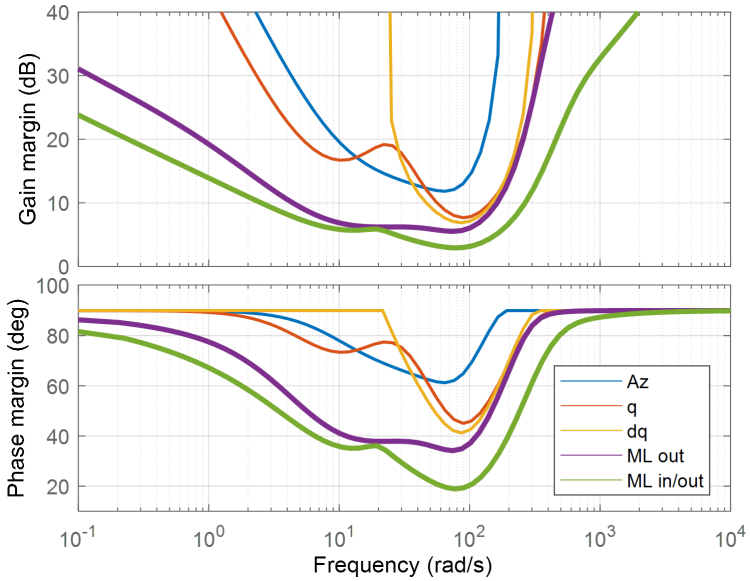

Fig. 9 Example stability margin plot

Table 2 Disk margin tuning goal

	$\alpha \leq 1^o$	$1^o < \alpha \leq 12^o$
Gain margin	2dB	3dB
Phase margin	15^o	30^o

in MATLAB to set up for the optimization process. As the goal varies across the flight envelope in this example, the `varyingGoal` function is used to wrap the different margin tuning goals into one object for the solver.

4.1.2 Loop Shape

This methodology enforces another *hard constraint* on the open-loop gain profile within the optimization to achieve desirable reference tracking, disturbance rejection, and noise attenuation properties. For this analysis, the feedback loop of the combined closed-loop system is broken, as shown in Fig. 10, and open-loop gain response (L) is shaped by analyzing the sensitivity (S) and complementary sensitivity (T) functions. Note the sensitivity and complementary sensitivity functions are restricted by the trade-off given by $S + T = 1$.

Figure 11 provides an example plot showing the open-loop gain, along with S and T. The target loop shape that of a pure integrator, and is enforced by a low-frequency constraint on S and a high-frequency constraint on T. These constraints

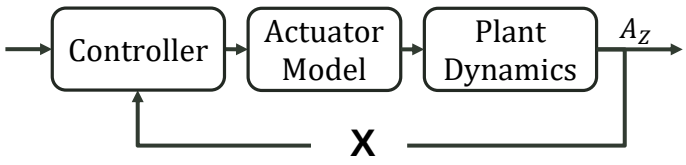

Fig. 10 Loop shaping analysis

are derived from the desired ω_c^{FC}. For frequencies below ω_c^{FC}, where $L > 1$, the green low-frequency keep-out region forces a minimum gain constraint on L (equivalently a max gain constraint on S) to provide desirable reference tracking performance and disturbance rejection. For frequencies greater than ω_c^{FC}, where $L < 1$, the red high-frequency keep-out region forces a maximum gain constraint on L and T to provide desirable noise attenuation. The gap between the two keep-out regions sets the frequency band where L can cross 0 dB, and is defined in this methodology by choosing the upper and lower frequency bounds as given in Table 3.

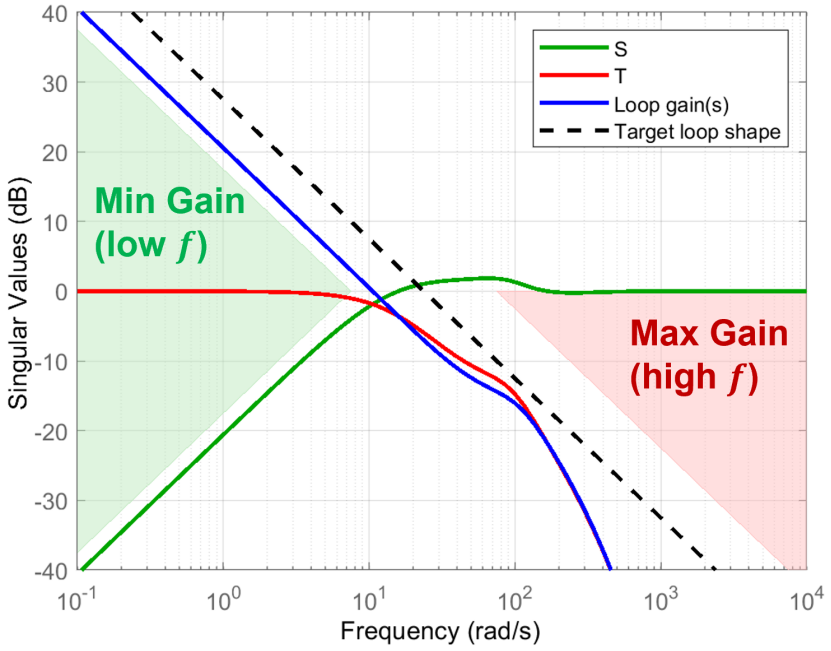

Fig. 11 Example loop gain plot, showing the sensitivity and complementary sensitivity functions

This design goal is implemented within MATLAB using `TuningGoal.LoopShape` to set up for the optimization process. As the goal varies across the flight envelope in this example (due to variations in ω_c^{FC}), the `varyingGoal` function is used to wrap the different loop shape tuning goals into one object for the solver.

Table 3 Loop shape tuning goal

	Min	Max
Crossover range	$0.5\omega_c^{FC}$	$5\omega_c^{FC}$

4.1.3 Reference Tracking

This methodology also enforces a *soft constraint* to optimize the reference tracking performance within the hard constraint limits. For this analysis, reference signals of varying frequency are provided to the closed-loop system, and the error between the reference and output is analyzed across frequency, as shown in Fig. 12.

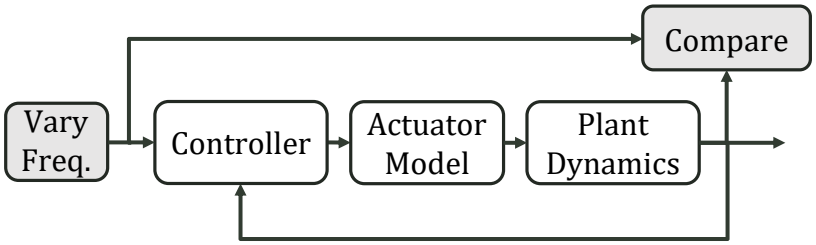

Fig. 12 Reference tracking analysis

Figure 13 provides an example plot showing the reference tracking goal. The relative error between the reference and response is plotted across frequency, and compared to a desired error profile with a 20-dB/decade slope consistent with an integrator response. The crossover frequency of the desired error profile in this example is set to ω_c^{FC}.

This design goal is implemented within MATLAB using the `TuningGoal.Tracking` function to set up for the optimization process. As the goal varies across the flight envelope in this example (due to variations in ω_c^{FC}), the `varyingGoal` function is used to wrap the varying reference tracking goal into one object for the solver.

4.2 Tuning Results

Once the tuning constraints are defined and implemented into MATLAB using `TuningGoal` and `varyingGoal` functions, and the K_a, K_i, K_q, and K_e gains within Eq. 38 have been set as `tunableSurface` functions according to Eq. 39, the problem is ready for optimization.

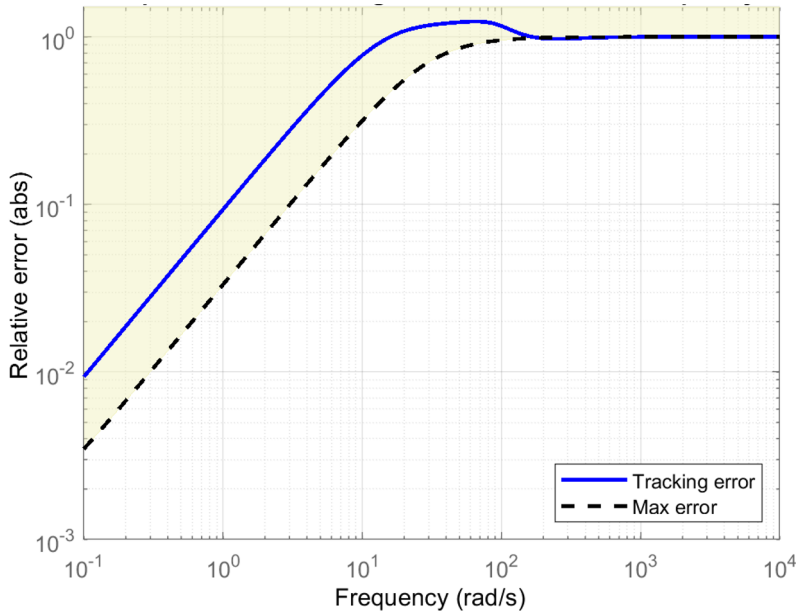

Fig. 13 Example reference tracking plot

The MATLAB `systune` function takes the closed-loop system model and the set of hard and soft constraints, and adjusts the surface coefficients for each gain to shape the surfaces in a way that satisfies the constraints across the flight envelope. Figure 14 shows the resulting tuned surfaces across the flight envelope for each tunable gain parameter in the controller.

The performance of the gain-scheduled controller is evaluated across the flight envelope to ensure desired robustness characteristics and performance. Using Eq. 38, the controller gain surfaces are evaluated at each sample point $\xi \in \Xi$ to obtain the family of tuned, closed-loop linearized models. These closed-loop systems are then compared to the tuning goal criteria.

Figure 15 plots the tuned system stability margins for each linear model and the corresponding controller gains across the flight envelope. The tuned gain surfaces result in a family of closed-loop systems that meet the design goals defined in Table 2 at each sample point within the flight envelope.

The open-loop gain profile for the family of tuned systems is shown in Fig. 16, along with the corresponding S and T function profiles. The tuned gain surfaces result in open-loop gain profiles, which meet the design goals defined in Table 3 at each sample point within the flight envelope.

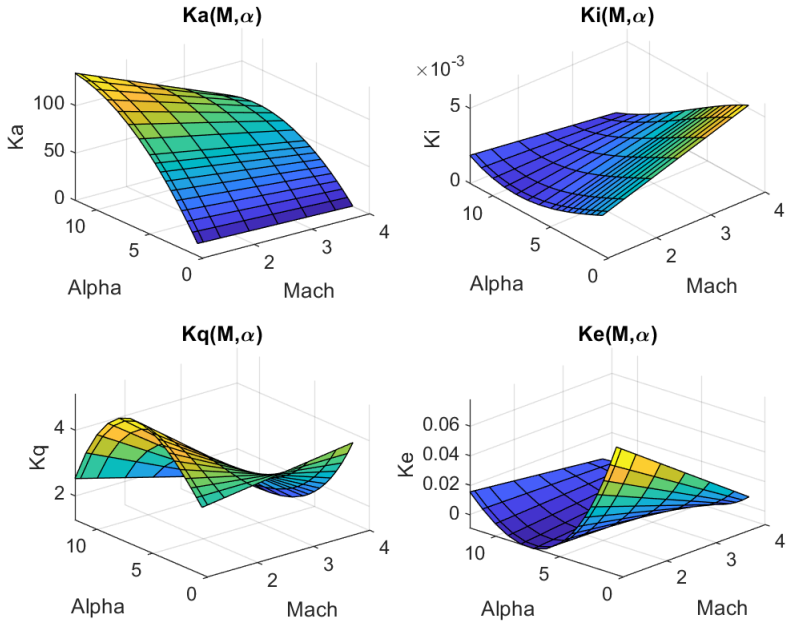

Fig. 14 Polynomial gain surfaces for K_a, K_i, K_q, and K_e

The family of closed-loop systems is further evaluated using a bode plot analysis and an analysis of the system response to step inputs, as shown in Figs. 17 and 18. These figures confirm the desired performance of the tuned, closed-loop systems at each sample point across the flight envelope. The effect of varying ω_c^{FC} according to Fig. 6 is evident in the Fig. 18 step responses, with lower Mach numbers corresponding to slower step responses.

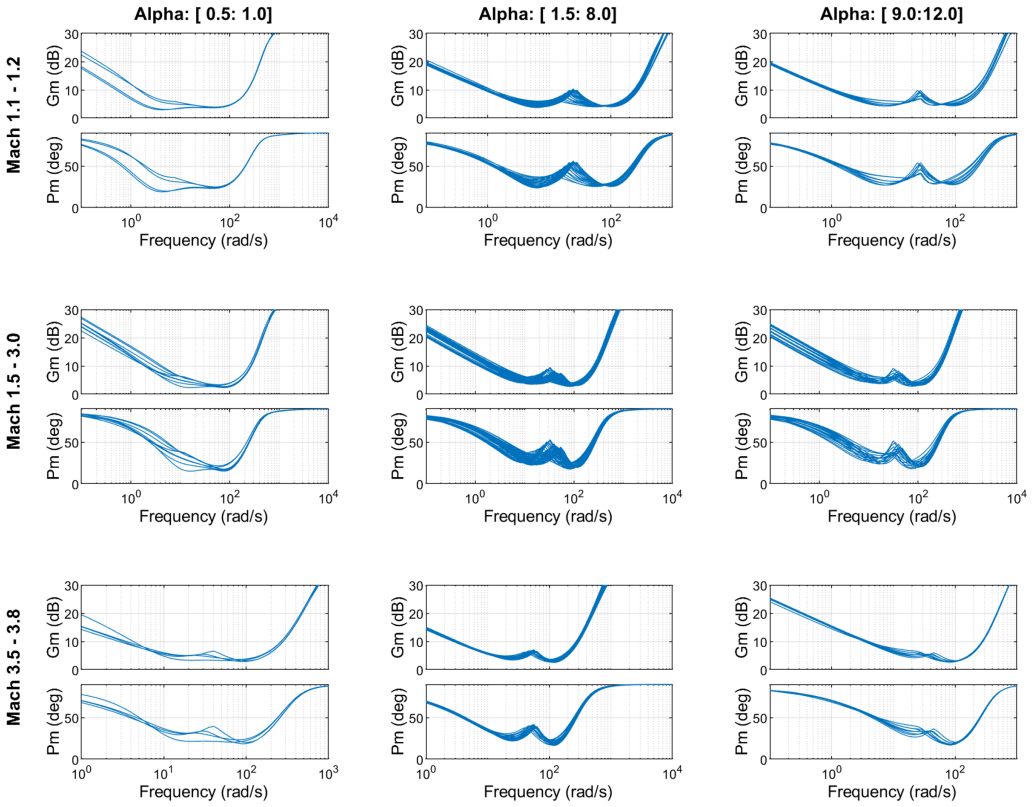

Fig. 15 Stability margins for the tuned, closed-loop system across the flight envelope

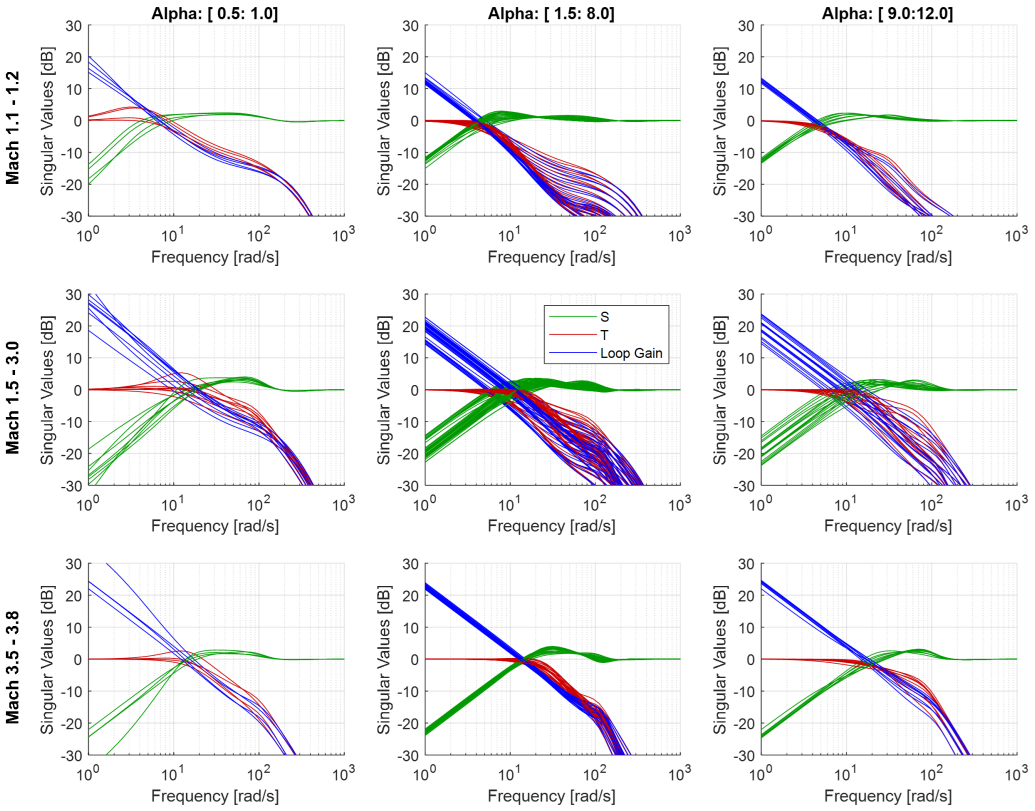

Fig. 16 Open-loop gain profiles for the tuned system across the flight envelope

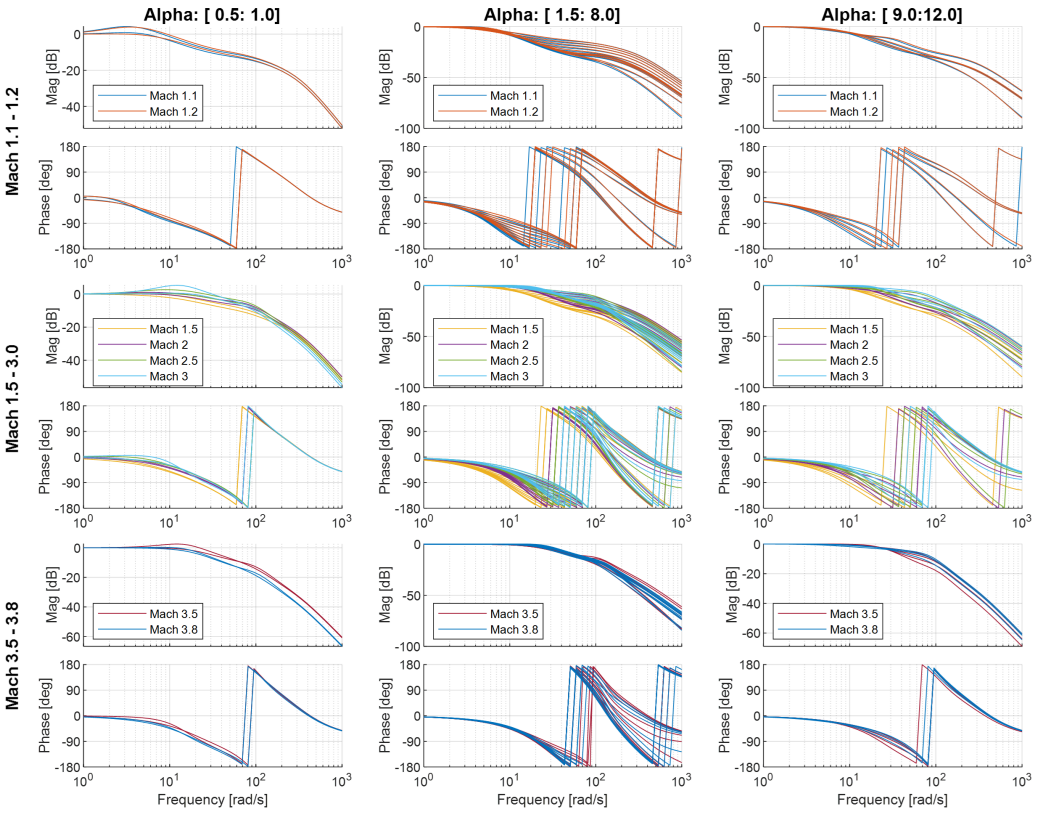

Fig. 17 Bode plots for the tuned, closed-loop system across the flight envelope

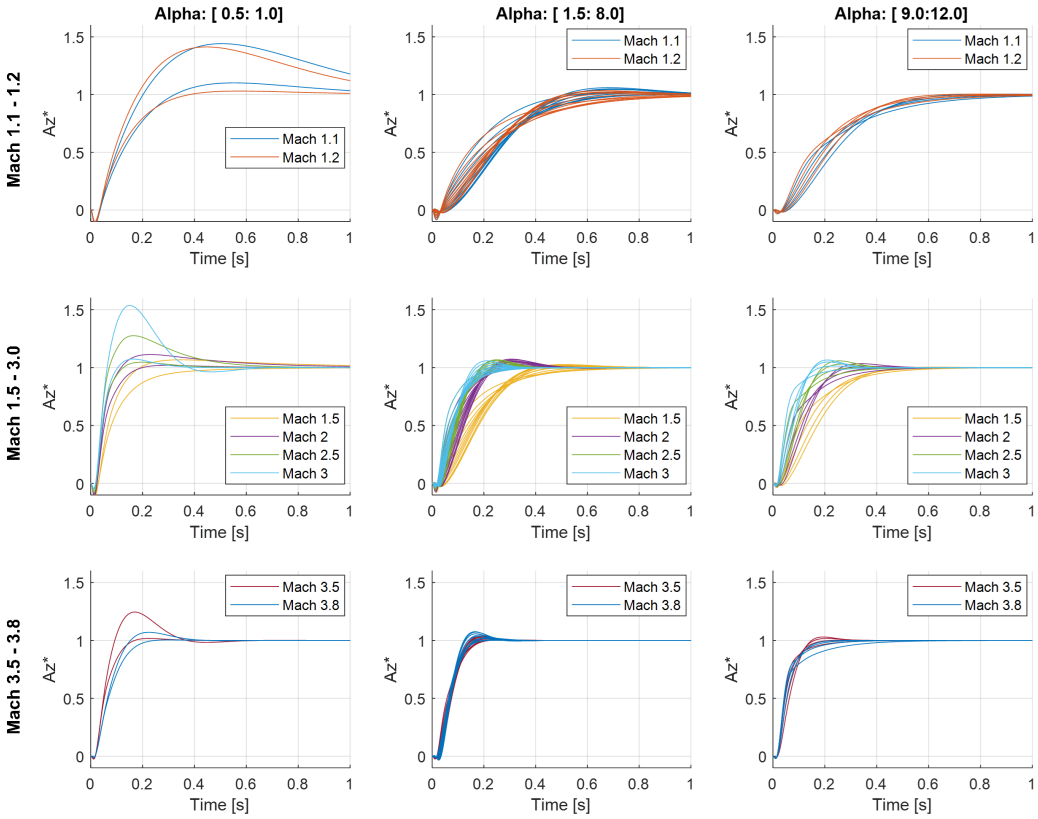

Fig. 18 Step responses of the tuned, closed-loop systems across the flight envelope

4.2.1 Nonlinear Simulation

The gain-scheduled flight controller is implemented in Simulink according to Fig. 5 with the tuned gain surfaces from Fig. 14. The flight controller is then simulated with the full nonlinear aerodynamics and equations of motion for the projectile in the longitudinal plane. An A_Z reference command is generated following a first-order response to a step input, with the reference model time constant, $\tau_R = 5$ rad/s, chosen to smooth/slow abrupt changes to the reference command below the ω_c^{FC}. Figure 19 plots the simulation results, showing the A_Z reference command and A_Z, α, q, simulation response, along with the control deflection, δ_q.

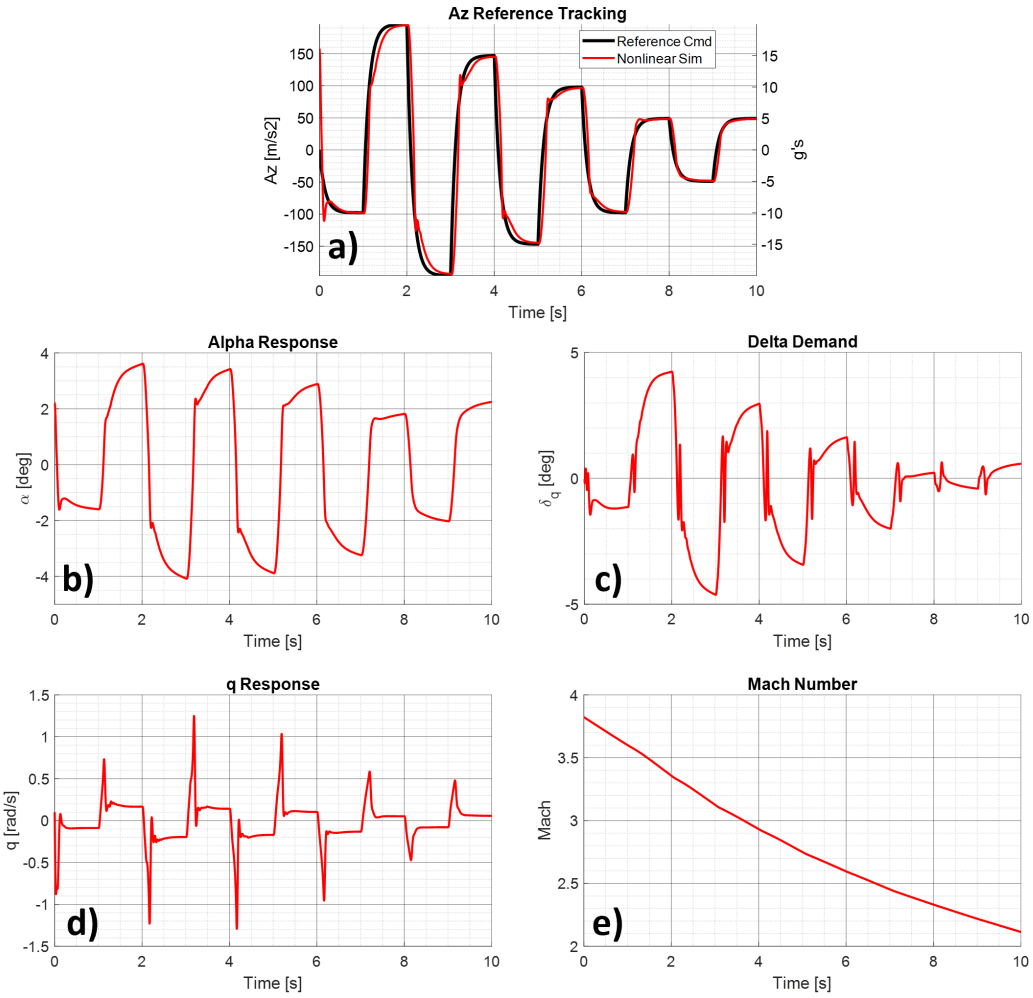

Fig. 19 Nonlinear simulation results with the tuned flight controller tracking an A_Z reference command

5. Robustness Analysis

The models used to design the flight controller are simplified expressions of the true dynamics, and hence, include errors and uncertainties that cause deviations from true flight behavior. The flight controller should be designed with robustness to this model error/uncertainty. One source of model error in this case is the linearization using the short-period approximation covered in Section 3, which neglects aspects of the nonlinear dynamics in order to make use of the powerful linear control design techniques. Additionally, the aerodynamic terms used within the model are obtained through the blending of multiple experimental and analytical techniques (CFD, wind tunnel, flight experiments, etc.), each of which have different strengths and limitations. This aerodynamic data fusion remains an area of active research, and the aerodynamic coefficients can have significant uncertainty, particularly in hypersonic flight regimes.

To add variability and uncertainty to the projectile and actuator dynamic models, the MATLAB `ureal` command is used to define *uncertain parameters*, which vary according to a specified error range. These uncertain parameters are used to rebuild the state-space models as *uncertain state-space models*, which contain the underlying uncertainty of the parameters within the differential equations. These uncertain models are then combined with the flight controller and used to analyze the robustness of the closed-loop system to the specified uncertainties.

5.1 Model Uncertainties

A conservative uncertainty bound is set for each parameter, as shown in Table 4. For this example, the projectile mass, m, and moment of inertia, I_y, are given an error bound of $\pm 10\%$ from their nominal values. The x-location of projectile center-of-gravity (CG) is assumed to vary by ± 0.1 cal. The air density, ρ, is given an error of $\pm 20\%$, and the projectile velocity, V, is given a $\pm 10\%$ uncertainty. These combine together to define the uncertainty in the dynamic pressure, $Q = 1/2\rho V^2$.

The aerodynamic force coefficients $C_{Z_\alpha}, C_{Z_\delta}$ are both given an error bound of $\pm 10\%$, and the error in the damping coefficient, C_{m_q} is assumed to be $\pm 30\%$, as shown in Table 4. The aerodynamic moment coefficients are affected by the CG uncertainty, along with an assumed additional error bound of $\pm 20\%$. The aerodynamic coefficient values vary across the flight envelope, so these error boundaries

Table 4 Dynamic model uncertainty bounds

Mass properties		Environment parameters		Aerodynamic coefficients		Actuator properties	
m	$\pm 10\%$	ρ	$\pm 20\%$	C_{Z_α}	$\pm 10\%$	ω_{n}	[280:350] rad/s
I_y	$\pm 10\%$	V	$\pm 10\%$	C_{Z_δ}	$\pm 10\%$		
CGx	± 0.1cal			C_{m_α}	$\pm 20\%$ ± 0.1 cal		
				C_{m_δ}	$\pm 20\%$ ± 0.1 cal		
				C_{m_q}	$\pm 30\%$		

are implemented as error surfaces derived from the nominal values, as shown in Fig. 20. Note the effect of the CG shift on the aerodynamic moments is cumulative with the $\pm 20\%$ error.

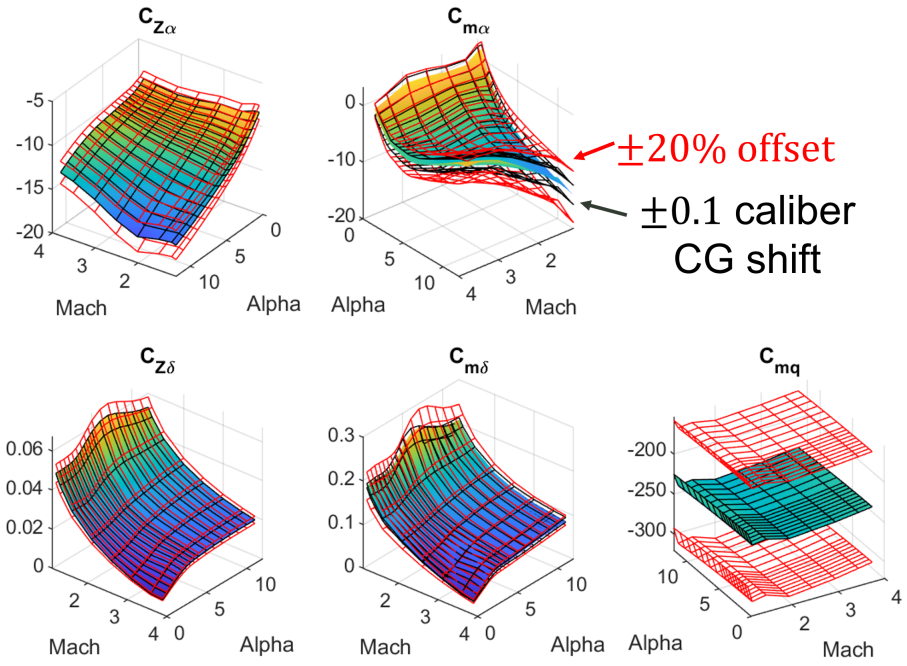

Fig. 20 Aerodynamic coefficients with uncertainty bounds (shown in red) around nominal values across flight envelope

The actuator response is also assumed to be uncertain, with a ω_{n} varying from 280 to 350 rad/s. This assumption captures uncertainties due to simplifications between the true dynamics and the second-order modeling approximation, as well as non-linearities in the actuator response in the presence of significant hinge moments due to aerodynamic forces on the control surfaces in high dynamic pressure flight conditions.

5.2 Robustness Analysis Results

Each of the parameters in Table 4 is defined with the MATLAB `ureal` command as an uncertain parameter with the associated uncertainty bounds. The actuator model from Eq. 36 is rebuilt using the uncertain ω_{n} value, resulting in an uncertain state-space model for the actuator. Similarly, the projectile dynamics model from Eq. 35 is rebuilt at each sample point across the flight envelope, resulting in a family of uncertain state-space models spanning the flight envelope, which each contain uncertain parameters bounded according to Table 4 and Fig. 20. The uncertain actuator model and uncertain projectile models are connected with the tuned flight controller to rebuild the closed-loop system in preparation for the robustness analysis, as illustrated in Fig. 21.

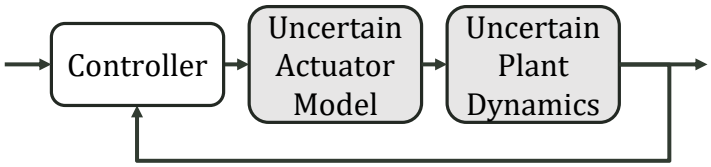

Fig. 21 Closed-loop model with uncertainty for robustness analysis

In this methodology, the robustness of the closed-loop system is evaluated using *μ-analysis*, which determines the minimum stability margin across frequency using the structured singular value, μ, for the uncertainty space defined in Table 4. This calculation is performed using the MATLAB `robstab` command and gives a deterministic calculation of stability across the defined uncertainty space using a *robustness factor*. This robustness factor (RF) indicates the stability of the system relative to the normalized uncertainty space, with $\mathrm{RF} = 1$ indicating the closed-loop system is robust to uncertainties that exactly match the error boundaries given, and $\mathrm{RF} > 1$ indicates the system is robust to uncertainties in excess of the specified error bounds.

For this example, the RF for the uncertainty space defined in Table 4 is shown in Fig. 22, which indicates this flight control design is robust to specified uncertainties across the majority of the flight envelope. At lower Mach numbers, the closed-loop system is shown to be robust to 150%–200% of the normalized uncertainty space. A few corner cases at low-α, low/high Mach are shown to be robust to only 70% of the specified error. This is a result of the relaxed stability margin tuning goal for those cases (see Table 2). If the robustness of these corner cases is insufficient,

the controller gain surfaces must be re-tuned with adjusted tuning goals. For this example, the robustness of the design is assumed to meet requirements.

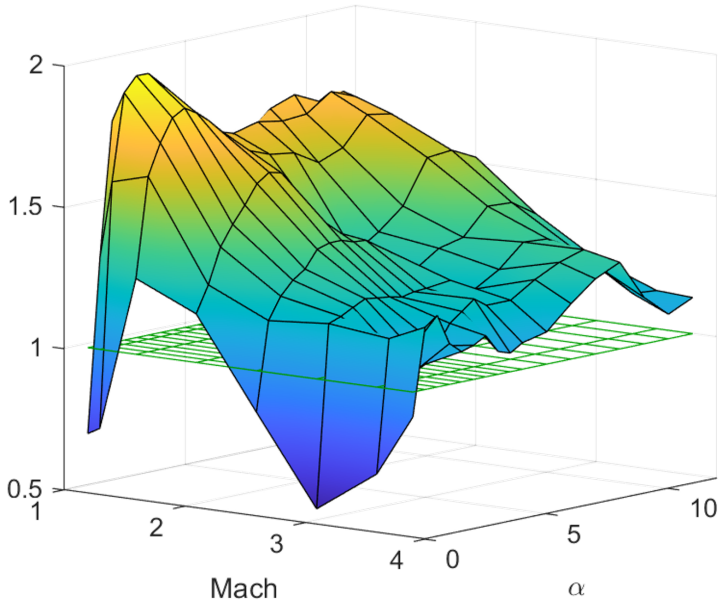

Fig. 22 RF calculated for the close-loop system, indicating stability with respect to the defined uncertainty space

The robustness analysis in this methodology also includes a measure of the relative effect of parameter variation on the stability. Figure 23 plots a line for each uncertain parameter in the analysis that shows the minimum, maximum, and average sensitivity of the closed-loop stability across the flight envelope to variations in that parameter across the specified error boundary. This comparison highlights which parameters most affect stability within the uncertainty bounds. For this example, the main drivers of stability are 1) CG offset errors, 2) airspeed and air density estimates (which combine into Q), and 3) actuator bandwidth. It should be noted that the relative sensitivity metric is a combination of the impact of each parameter on stability as well as the size of the corresponding error space. Parameters can be key drivers due to large uncertainty bounds and/or out-sized impact on stability. For example, the CG offset parameter has significant impact on stability from first principles and was given a large uncertainty range in this example, so its role as a driver in this analysis is expected. In contrast, the actuator bandwidth was given a relatively small uncertainty range in this analysis, yet shows up as a significant driver of instability, highlighting the critical role the actuator performance plays in closed-loop system stability.

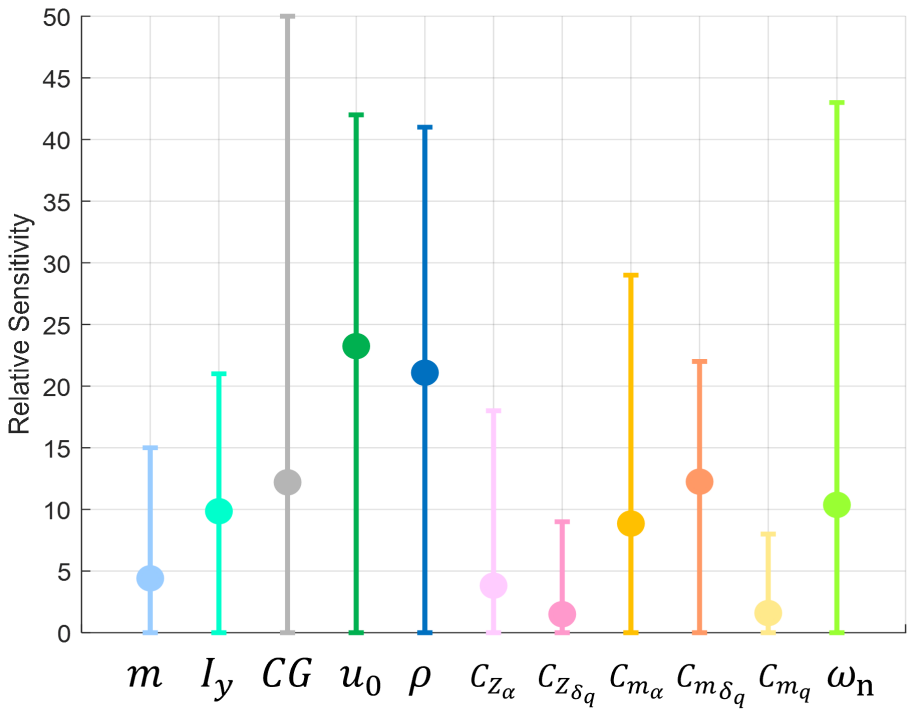

Fig. 23 Measure of the relative effect of variation in each parameter on stability

5.3 Nonlinear Simulation

As part of the overall robustness analysis, the scheduled flight controller is exercised in a Monte Carlo (MC) simulation using the full nonlinear aerodynamic model and pitch plane equations of motion. This MC analysis provides a complement to the RF analysis to ensure the linearization assumptions and flight envelope sampling have not missed critical details.

Uniform random draws are taken for each uncertain parameter according to the error bounds defined in Table 4, and each case is exercised in simulation. The controller is provided an A_Z reference command to track, and the initial conditions are chosen to exercise the controller across the majority of the (Mach, α) pair values within the flight envelope. The flight behavior for 150 simulations is shown in Fig. 24. As the uncertain parameters deviate from their nominal values, the controller continues to provide acceptable A_Z tracking performance, with the δ_q commands and α responses adjusting from their nominal values to accommodate the changing dynamics.

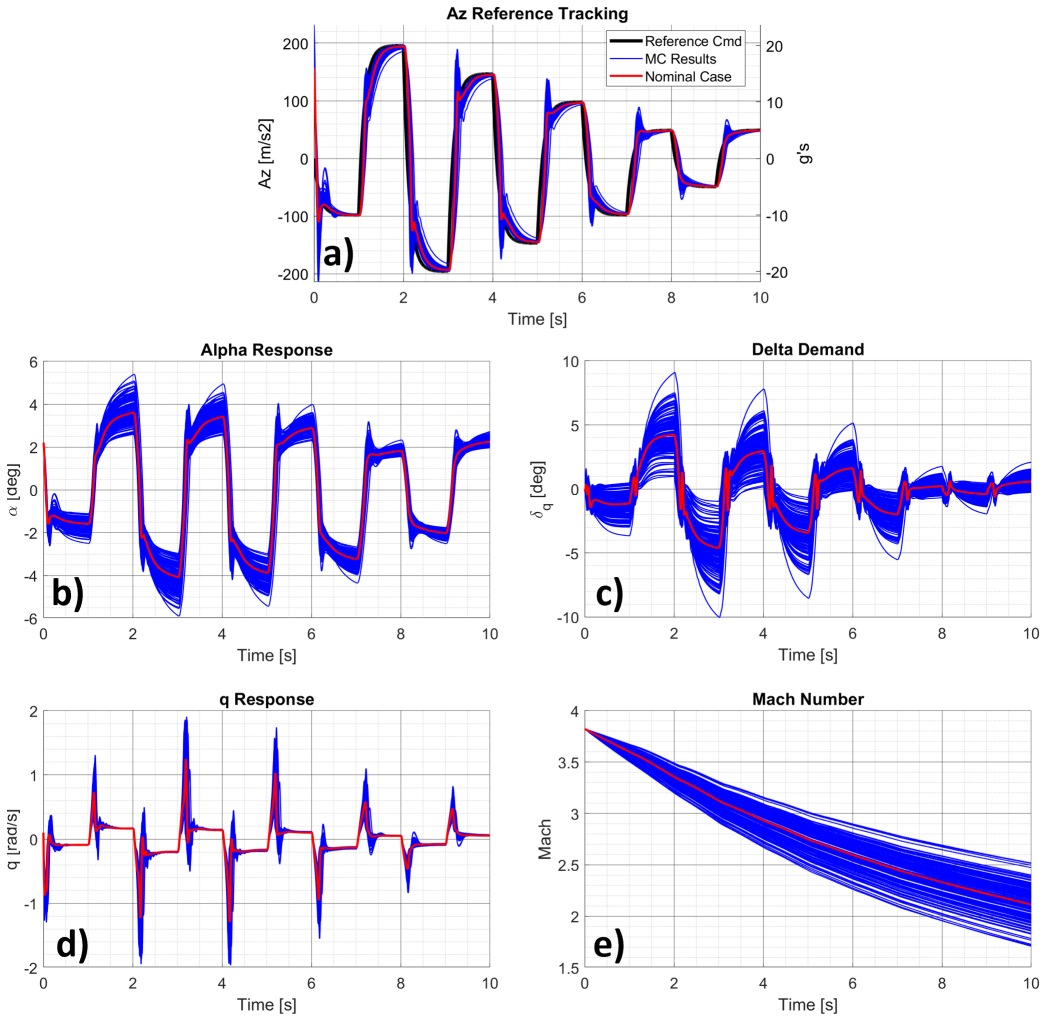

Fig. 24 MC simulation results using the nonlinear flight dynamic model

6. Conclusion

A flight control design methodology was developed that provides effective disturbance rejection and command tracking for a high-speed guided munition across an expanded flight envelope, while prioritizing robustness to modeling uncertainties and maintaining a focus on rapid tuning capability by leveraging available tools for automation. This efficient, systematic tuning approach was used to gain-schedule a three-loop autopilot for an example tail-controlled projectile, using a set of desired design constraints to enforce performance, stability, and robustness properties.

The performance of the resulting closed-loop system was evaluated using a variety of linear systems analysis techniques to verify the tuning goals were satisfied. Nonlinear simulation results of the closed-loop system were presented to illustrate performance across the flight envelope.

A robustness analysis was performed, which verified the closed-loop system to be robust to significant errors/uncertainties in the model parameters. This robustness analysis was complemented with nonlinear simulation results from a MC analysis that varied each model parameter across its uncertainty boundary and showed the closed-loop system exhibits a graceful degradation in performance across the defined modeling uncertainty space.

7. References

1. US Army Training and Doctrine Command (TRADOC). The U.S. Army in Multi-Domain Operations 2028. 2018 Dec. Pamphlet No.: 525-3-1.

2. Vasile JD, Bryson J, Fresconi F. Aerodynamic design optimization of long range projectiles using missile datcom. AIAA Scitech 2020 Forum; 2020 Jan. Paper No.: AIAA 2020-1762.

3. Vasile JD, Bryson J, Gruenwald BC, Fairfax L, Strohm L, Fresconi F. A multi-disciplinary approach to design long range guided projectiles. AIAA Scitech 2020 Forum; 2020 Jan. Paper No.: AIAA 2020-1993.

4. Bryson J, Vasile JD, Gruenwald BC, Fresconi F. Control surface design analysis and actuation requirements development for munitions. AIAA Scitech 2020 Forum; 2020 Jan. Paper No.: AIAA 2020-0020.

5. Gruenwald BC, Bryson J. Adaptive control for a guided projectile using an expanded reference model. AIAA Scitech 2020 Forum; 2020 Jan. Paper No.: AIAA 2020-1822.

6. Fairfax LD, Vasile JD, Strohm L, Fresconi F. Trajectory shaping for quasi-equilibrium glide in guided munitions. AIAA Scitech 2020 Forum; 2020 Jan. Paper No.: AIAA 2020-0021.

7. Theodoulis S, Proff M. Robust flight control tuning for highly agile missiles. AIAA Scitech 2021 Forum; 2021 Jan. Paper No.: AIAA 2021-1568.

8. Stengel RF. Flight dynamics. Princeton University Press; 2015.

9. Schmidt LV. Introduction to aircraft flight dynamics. AIAA; 1998.

10. Cook MV. Flight dynamics principles: a linear systems approach to aircraft stability and control. Butterworth-Heinemann; 2012.

11. Zipfel P. Modeling and simulation of aerospace vehicle dynamics, third edition. American Institute of Aeronautics, Inc.; 2014.

12. Fresconi F, Celmins I, Silton S, Costello M. High maneuverability projectile flight using low cost components. Aerospace Science and Technology. 2015;41:175–188.

13. Burchett BT, Vasile JD, Bryson J. Combining sparse and dense databases to form a robust aerodynamic model for a long-range, high-speed projectile. AIAA Scitech 2022 Forum; 2022 Jan. Paper No.: AIAA 2022-0419.

14. Vasile J, Sahu J. Roll orientation–dependent aerodynamics of a long-range projectile. DEVCOM Army Research Laboratory; 2020 Aug. Report No.: ARL-TR-9017.

15. Gruenwald BC, Bryson J. Direct uncertainty minimization adaptive control for a guided projectile. AIAA Scitech 2021 Forum; 2021 Jan. Paper No.: AIAA 2021-0783.

16. Bryson J, Vasile JD, Gruenwald BC, Saju J, Fresconi F. Modeling and flight dynamics of a projectile with nonlinear, roll-dependent aerodynamics. AIAA Scitech 2021 Forum; 2021 Jan. Paper No.: AIAA 2021-0823.

17. Bryson J, Gruenwald BC. Linear parameter varying model predictive control of a high-speed projectile. AIAA Scitech 2022 Forum; 2022 Jan. Paper No.: AIAA 2022-1585.

18. Gruenwald BC, Bryson J. A gain-scheduled approach for the control of a high-speed guided projectile. AIAA Scitech 2022 Forum; 2022 Jan. Paper No.: AIAA 2022-0612.

List of Symbols, Abbreviations, and Acronyms

CG	center-of-gravity
MATLAB	MATrix LABoratory
MC	Monte Carlo
MDO	Multi-Domain Operations
LRPF	Long-Range Precision Fires
RF	robustness factor

MATHEMATICAL OPERATORS:

$([T]^{AB})$	denotes a transformation matrix that gives reference frame A with respect to reference frame B.
$(\dot{})$	the overdot denotes the time-derivative.
$(\vec{})$	the over arrow denotes a vector.
$(\cdot)^{\mathrm{T}}$	the transpose operator.
$(\times)$	denotes the cross product.
$(\cdot)^{-1}$	the inverse operator.

1 (PDF)	DEFENSE TECHNICAL INFORMATION CTR DTIC OCA
1 (PDF)	DEVCOM ARL FCDD RLD DCI TECH LIB
18 (PDF)	DEVCOM ARL FCDD RLW A F E FRESCONI FCDD RLW W T SHEPPARD FCDD RLW WD J T BRYSON B C GRUENWALD L STROHM B BURCHETT I CELMINS J DESPIRITO L FAIRFAX J PAUL J D VASILE FCDD RLW WA N TRIVEDI FCDD RLW WB J SADLER FCDD RLW WC M MINNICINO FCDD RLW WE M ILG B TOPPER J MALEY FCDD RLW WF E RIGAS